JOURNAL OF GEOPHYSICAL RESEARCH, VOL. 114, B02202, doi:10.1029/2008JB005722, 2009

Global Positioning System detection and energy estimation of the ionospheric wave caused by the 13 July 2003 explosion of the Soufrière Hills Volcano, Montserrat

Thomas Dautermann,[1,2] Eric Calais,[3] and Glen S. Mattioli[4]

Received 27 March 2008; revised 2 September 2008; accepted 14 October 2008; published 5 February 2009.

[1] Volcanic explosions or shallow earthquakes are known to trigger acoustic and gravity waves that propagate in the atmosphere at infrasonic speeds. At ionospheric heights, coupling between neutral particles and free electrons induces variations of electron density detectable with dual-frequency Global Positioning System (GPS) measurements. Using GPS data collected in the Caribbean, we identified an ionospheric perturbation after a major volcanic explosion at the Soufrière Hills Volcano (Montserrat, Lesser Antilles) on 13 July 2003. Spectral analysis reveals peaks centered at 1 and 4 mHz, similar to those in previous observations and consistent with theory, suggesting both gravity and acoustic wave components. We retrieve a horizontal velocity of $\sim$624 m/s for the acoustic component, which implies upward propagation at $\sim$33°, consistent with ray-tracing results. We model the acoustic wave using an *N*-wave pressure source at ground level combined with ray tracing to propagate the neutral pressure wave; this accounts for the dispersive characteristics of the atmosphere while conserving total acoustic energy. Plasma velocity is derived from neutral velocity using a finite difference solution of the magnetohydrodynamic momentum equation. The continuity equation for charge densities is used to compute corresponding electron density variations, which are then numerically integrated along satellite-to-receiver line of sights, simultaneously accounting for the satellite displacements. We minimize the misfit between observed and model waveforms to estimate a total acoustic energy release of 1.53×10^{10} J for the primary explosion event at Soufrière Hills Volcano associated with the peak dome collapse. This method can be applied to any explosion of sufficient magnitude, provided GPS data are available at near to medium range from the source.

Citation: Dautermann, T., E. Calais, and G. S. Mattioli (2009), Global Positioning System detection and energy estimation of the ionospheric wave caused by the 13 July 2003 explosion of the Soufrière Hills Volcano, Montserrat, *J. Geophys. Res.*, *114*, B02202, doi:10.1029/2008JB005722.

1. Introduction

[2] Subsurface and atmospheric explosions, large volcanic eruptions, strong earthquakes, and rocket launches have been shown to generate atmospheric infrasonic acoustic and gravity waves, which can propagate over great distances. For instance, *Yamamoto* [1956] describes atmospheric pressure oscillations at ground level in Japan caused by a hydrogen bomb detonation in the Marshall island about 4,000 km away. *Widmer and Zürn* [1992] and *Zürn and Widmer* [1996] show long-period atmospheric pressure oscillations triggered by the Pinatubo (Philippines) and El Chichon (Mexico) volcanic explosions recorded 9,000 and 3,000 km away.

[3] As these perturbations propagate upward, they eventually reach the ionospheric layers, where neutral particle flow couples with ionized plasma, inducing fluctuations of the ionospheric electron density [e.g., *Yeh and Liu*, 1972]. Because density decreases (quasi-exponentially) with altitude energy conservation implies that the perturbation amplitude increases by a factor of $\sim 10^4$ at ionospheric heights for a near-surface source. The resulting electron density perturbation may therefore become detectable using ground- or space-based observations [*Blanc*, 1985].

[4] The Global Positioning System (GPS) provides a straightforward way of measuring electron density and its variations because the differential signal delay of its two carrier frequencies is proportional to the path integral of the electron density (or Total Electron Content = TEC) from GPS satellites to receiving stations [*Klobuchar*, 1985]. GPS-derived TEC measurements have been used to detect and quantify ionospheric perturbations caused by explosions

[1]Department of Physics, Purdue University, West Lafayette, Indiana, USA.
[2]Now at Institute of Communications and Navigation, German Aerospace Center (DLR), Wessling, Germany.
[3]Department of Earth and Atmospheric Sciences, Purdue University, West Lafayette, Indiana, USA.
[4]Department of Geosciences, University of Arkansas, Fayetteville, Arkansas, USA.

0148-0227/09/2008JB005722$09.00

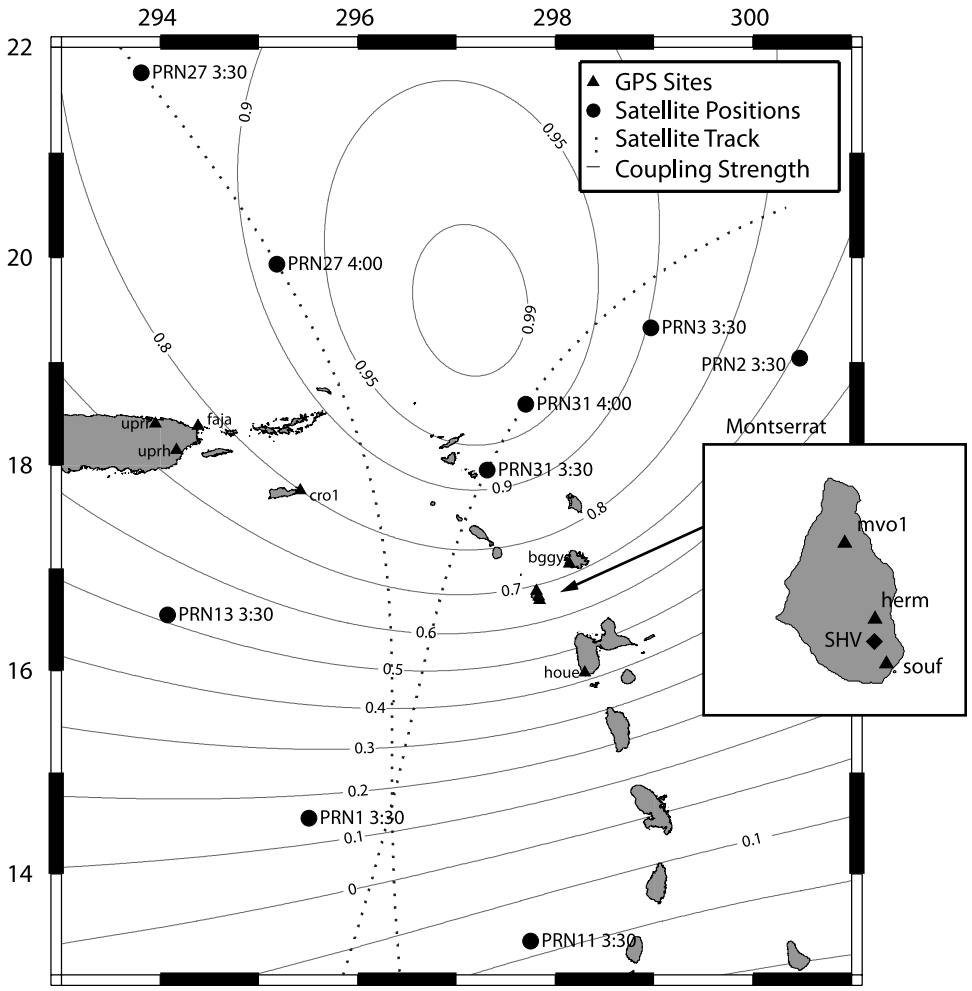

Figure 1. Map of the northeastern Caribbean showing the GPS sites used in this study (triangles). Dotted lines show the subionospheric point (SIP) traces for GPS satellites PRN27 and 31. Black circles mark the SIP of the satellites visible at the time of the explosion (with corresponding UT time indicated). Thin solid lines labeled from 0 to 1 are the contours of a proxy for the coupling efficiency between the neutral pressure wave and the ionospheric electron density variation (explanations in text). Note that only PRN27 and PRN31 are in areas of high coupling after the explosion.

and earthquakes. For instance, *Fitzgerald* [1997] describes the TEC perturbation caused by the 8.5×10^{12} J Minor Uncle blast in 1993 and shows that the source is well matched by an "*N*-wave" pulse. *Calais et al.* [1998] describe the TEC perturbation caused by a 6.3×10^{12} J mining explosion and models its propagation using a ray-tracing technique. Volcanic explosions are also powerful sources that can trigger TEC perturbations. Before the advent of GPS, *Roberts et al.* [1982] reported ionospheric perturbations caused by the 1980 eruption of Mount St. Helens using integrated electron content data from ATS satellites. More recently, *Heki* [2006] used GPS-derived TEC from the Japanese Geonet GPS network to quantify the explosion energy of the Asama volcano explosion of 1 September 2004.

[5] Here, we use GPS data to quantify the atmospheric perturbation caused by the 13 July 2003, primary explosion of the Soufrière Hills volcano on Montserrat (Lesser Antilles) associated with the peak lava dome collapse [*Herd et al.*, 2005]. We model the resulting acoustic wave using ray tracing and estimate the explosion acoustic energy. In particular, we show that the long wave train observed at near-field stations requires that the dispersion characteristics of the acoustic pulse be included in the model.

2. Data

[6] The Soufrière Hills Volcano (SHV) on Montserrat, located between Guadeloupe and Antigua in the Lesser Antilles (Figure 1), erupted on 13 July 2003 with an explosive lava dome collapse (Figure 2). A detailed description of the sequence of events, which eventually culminated in the 0.210 km^3 volcanic dome collapse and associated explosion at 3:35 UTC can be found in the study of *Herd et al.* [2005]. At the time, Montserrat was instrumented with GPS stations as part of the Caribbean Andesite Lava Island Precision Seismo-geodetic Observatory (CALIPSO [*Mattioli et al.*, 2004]). Additionally, data from permanent GPS sites throughout the Caribbean were also available, for a total

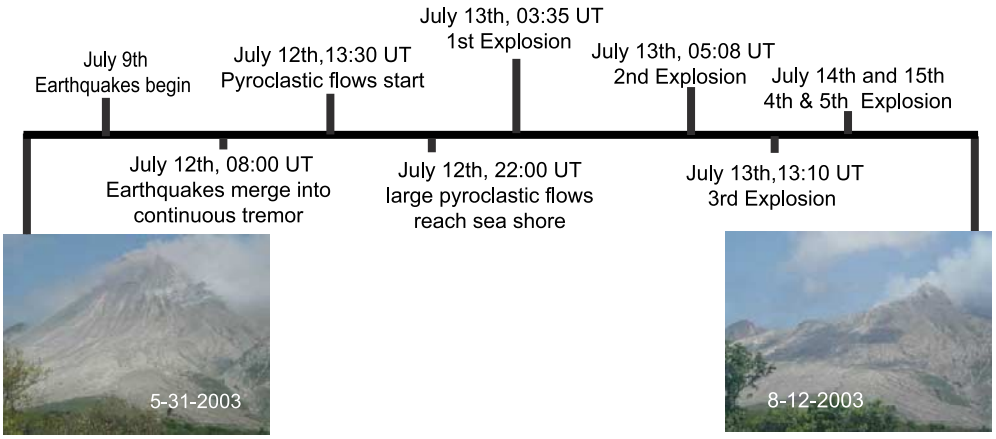

Figure 2. Abbreviated sequence of the SHV eruption following *Herd et al.* [2005]. The two pictures show the SHV dome in May 2003 before the dome collapse and in August 2003 after the dome collapse due, for the most part, to the 13–15 July explosions. According to *Mattioli et al.* [2007], the pyroclastic flows generated by dome collapse events of 12 and 13 July caused a small tsunami recorded on Montserrat by bore hole sensors and through direct observation on Guadeloupe.

of 9 sites within 600 km of Montserrat, all operating at a sampling rate of T_s = 30 s.

[7] The differential delay between the GPS phase observables Φ_1 and Φ_2 on the two GPS frequencies f_1 = 1575.42 MHz and f_2 = 1227.6 MHz is proportional to the path integral of electron density $N(\vec{r})$ along the propagation path of the GPS signal, also called Total Electron Content or TEC [e.g., *Klobuchar*, 1985]:

$$TEC = \int_{Receiver}^{Satellite} N(\vec{r})d\vec{r} \qquad (1)$$

[8] TEC is commonly measured in TECU (1 *TECU* = 10^{16} *electrons*/m^2) and calculated from the GPS observables using

$$TEC = \left(\Phi_2 - \frac{f_2}{f_1}\Phi_1 + n + f_2(b_r + b_s)\right)\frac{f_1^2 f_2}{f_1^2 - f_2^2}\frac{c_l}{A} \qquad (2)$$

with A = 40.3 m^{3}s^{-2} and c_l is the speed of light [e.g., *Manucci et al.*, 1993]. n is a constant offset for each orbital arc caused by the initial lock onto the signal (phase ambiguities). b_r and b_s are code delays specific to receiver and satellite hardware, respectively. These biases can be estimated from the data [*Sardon et al.*, 1994; *Mazzella et al.*, 2002] but will not be considered in the present analysis since we are interested in temporal variations of TEC rather than absolute TEC.

[9] We apply this straightforward calculation to dual-frequency GPS data from the 9 GPS sites available in the Caribbean at the time of the explosion (Figure 1) and map the TEC to the vertical in order to account for the different path lengths of the signal through the ionosphere as the satellite elevation changes. Each TEC measurement is associated with a subionospheric point (SIP), defined as the ground projection of the intersection between the receiver-satellite line of sight and the peak electron density height (325 km).

[10] Figure 3a shows the unfiltered TEC time series derived at site MVO1 for satellite PRN27 on 13 July 2003, with the same analysis for 12 July shown for comparison (no data was recorded at MVO1 on 14 July because of the power outage caused by the eruption). Distinct oscillations with a period of about 12 min (frequency 1.4 mHz) and amplitude of ~2 TECU are visible in the data, starting at 3:55 UTC (18 min after the explosion) and lasting for about 40 min. A spectral analysis of the TEC time series shows two peaks present on 13 July, but not on 12 July (Figure 3b). The larger amplitude one is centered at 1.4 mHz (see above), in the frequency range of gravity waves. A second one, of lower amplitude, is centered around 4 mHz, in the frequency range of acoustic waves. Spectral components of TEC data from 15 July are consistent with those from 12 July. Since ionospheric perturbations can be caused by enhanced solar activity and magnetic storms, we verified that geomagnetic indices from the U.S. National Geophysical Data Center (http://spidr.ngdc.noaa.gov, indices *Dst* and A_p) show no significant magnetic or solar flux disturbance on 13 July 2003.

[11] Data from a total of 7 satellites were available at the time of the primary SHV explosion at 3:35 UT, but we found a significant TEC perturbation on data from satellites 27 and 31 only, both located to the north of the explosion site (Figure 1). Direction sensitivity of TEC measurements has been previously reported [*Calais et al.*, 1998; *Heki and Ping*, 2005] and is likely due to the fact that charged particles in the F region move preferentially along magnetic field lines. The electron velocity follows approximately $v = v_n\cos(\alpha)$, where v_n is the neutral velocity and α the angle between the propagation direction of the acoustic perturbation and the magnetic field lines from *Georges and Hooke* [1970]. We computed "coupling coefficients" $\cos(\alpha) = \frac{\vec{v}\vec{B}}{|\vec{v}|\,|\vec{B}|}$ using magnetic field vectors $\vec{B}$ from the International Geomagnetic Reference Field IGRF-10 [*Maus and Macmillan*,

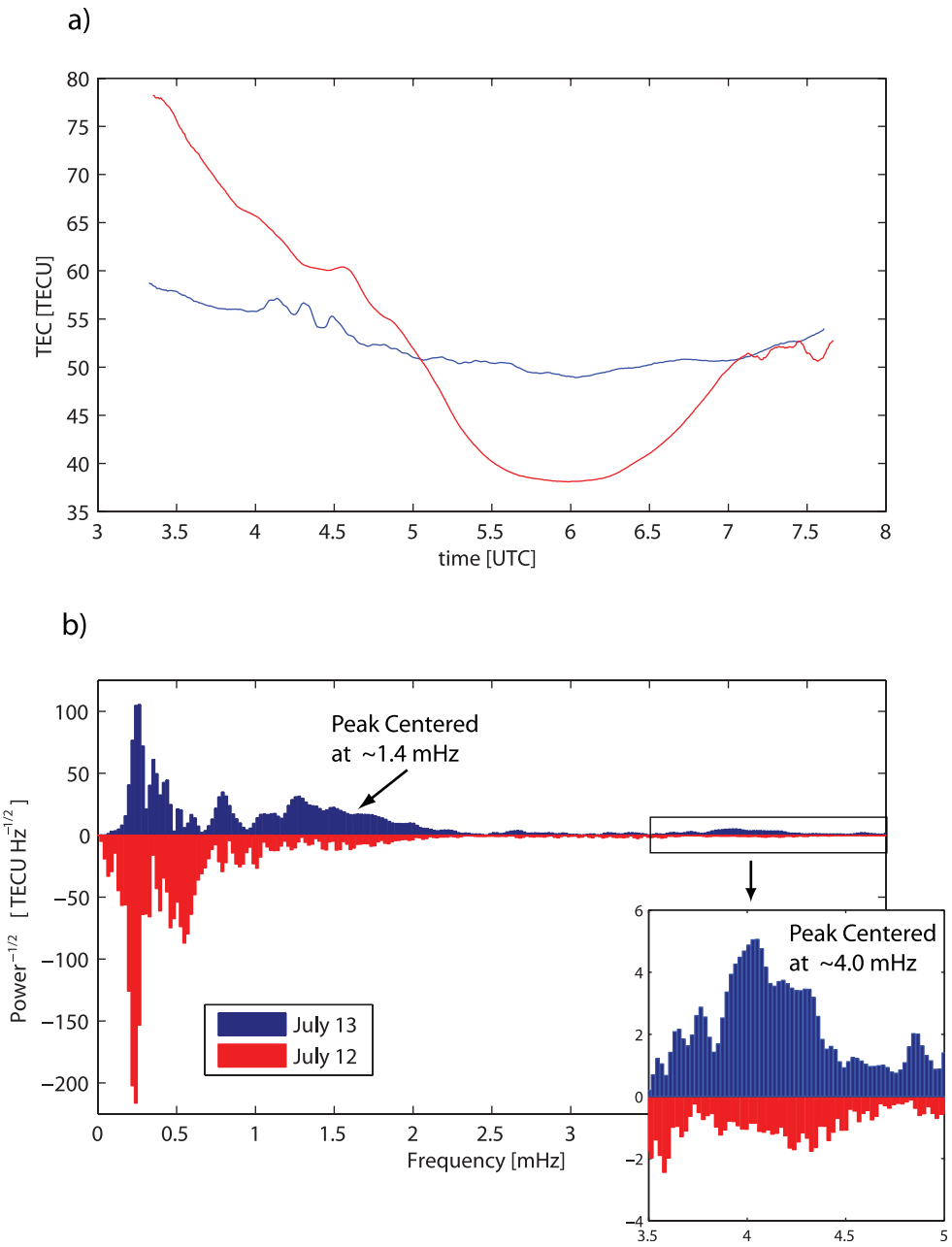

Figure 3. (a) Unfiltered TEC time series recorded along the line of sight from station MVO1 on Montserrat and satellite PRN27 for 13 July 2003 (day of the explosion, in blue) and 1 day earlier (in red). The long wavelength trend is the diurnal effect due to solar activity (local time is UTC-4). TEC perturbations are visible on 13 July starting around 4 UT. (b) Power spectrum of two distinct frequency components centered on 1.4 and 4.0 mHz are present on 13 July.

2005] and theoretical acoustic wave propagation direction $\vec{v}/|\vec{v}|$ from a ray-tracing model (using directions from 180 rays, see section 3.1) as the rays pierce through 325 km height (peak electron density). Figure 1 shows that the area of maximum coupling is located northwest of Montserrat, where SIPs corresponding to satellites 27 and 31 are located in the hours following the SHV explosion. Other satellites were visible at the same time, but located in sky quadrants where coupling efficiency between neutral perturbations and electron density changes is predicted to be low.

[12] In order to isolate the acoustic component of the TEC perturbation, we applied a zero-phase 4th-order Butterworth band-pass filter with cutoffs at 2.2 mHz (acoustic cutoff frequency) and 8 mHz (half the Nyquist frequency given the GPS sampling rate of 30 sec). The acoustic perturbation is visible on all time series for satellites 27 and 31 (Figure 4), starting about 15 minutes after the explosion at the closest SIPs (Guadeloupe). This is consistent with the 13 min theoretical propagation time of an acoustic perturbation from ground level straight up to the peak electron density at 325 km. Arrival times increase with distance to Montserrat,

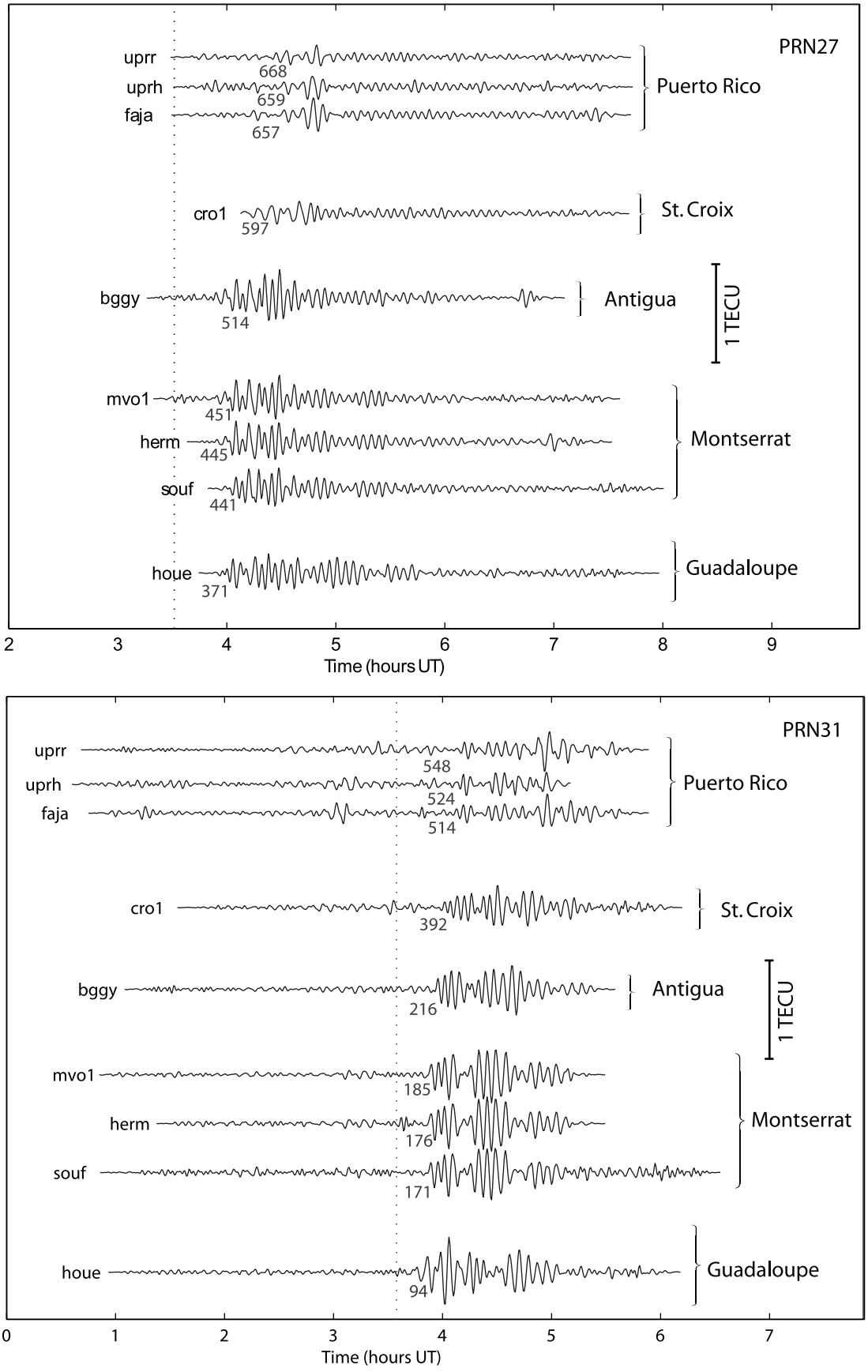
PRN27
uprr
668
uprh
659
faja
657
Puerto Rico
cro1
597
St. Croix
bggy
514
Antigua
1 TECU
mvo1
451
herm
445
souf
441
Montserrat
houe
371
Guadaloupe
2
3
4
5
6
7
8
9
Time (hours UT)
PRN31
uprr
548
uprh
524
faja
514
Puerto Rico
cro1
392
St. Croix
bggy
216
Antigua
1 TECU
mvo1
185
herm
176
souf
171
Montserrat
houe
94
Guadaloupe
0
1
2
3
4
5
6
7
Time (hours UT)

Figure 4

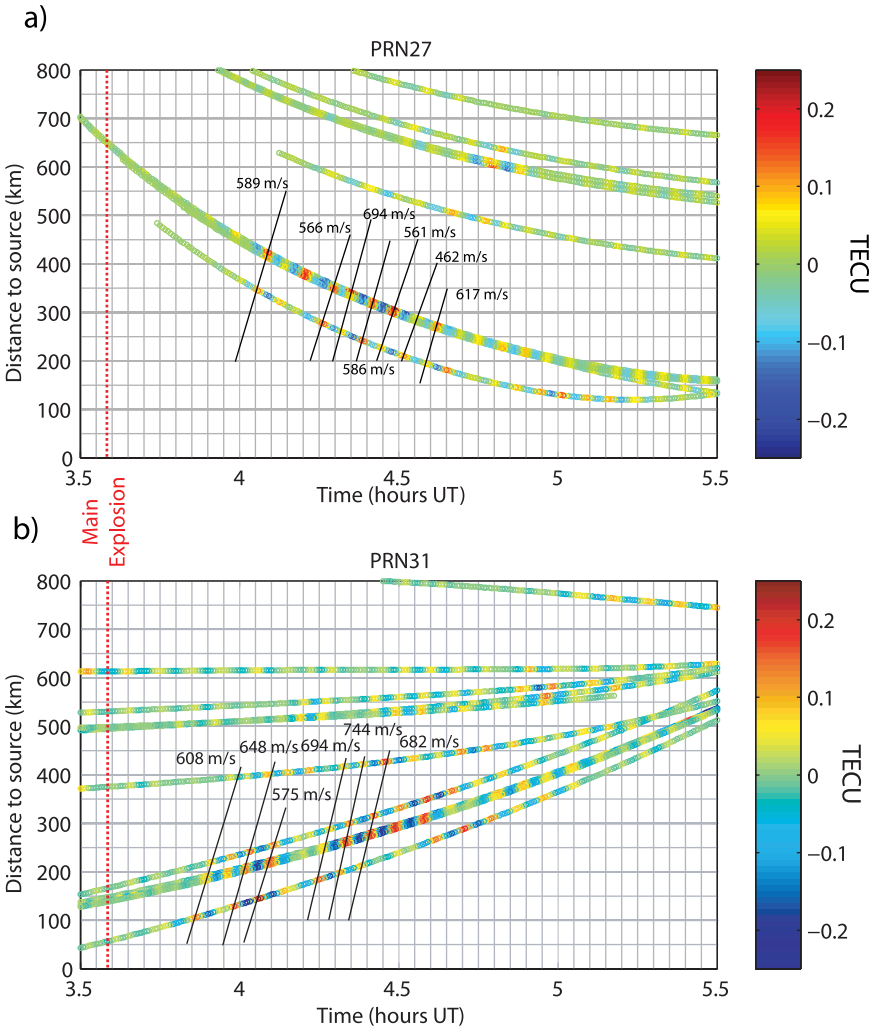

Figure 5. Filtered TEC traces shown in actual time-distance frame, i.e., accounting for the variable SIP-source distance as the satellite moves along its orbit.

illustrating outward propagation of the perturbation. The observed wave train lasts for about 1.5 hours at the closest SIPs with waveforms well correlated among groups of neighboring stations but more complex than the single N-shaped pulse observed by *Heki* [2006] or *Fitzgerald* [1997] for other volcanic explosions. At larger distances (e.g., Puerto Rico in Figure 4, top and bottom), the perturbation amplitude decreases and its duration appears to shorten, which likely results from signal attenuation below the background noise level. To test this, we computed the noise level as the variance of the TEC signal in the absence of a perturbation (using data from 12 July). We find that the signal-to-noise ratio decreases from 5 at the closest stations to the explosion to 1.2 at the farthest ones (Figure 4), thus resulting in TEC perturbation indistinguishable from background noise at sites located more than 500 km from the explosion (e.g., western Puerto Rico, Dominican Republic, and Florida, where continuous GPS sites show no detectable perturbation).

[13] Figure 5 shows the amplitude of the acoustic perturbation in a "true" time-distance diagram, i.e., accounting for the time dependence of the geometry of the SIPs. Again, the perturbation appears clearly between 04:00 and 05:00 UT, with multiple oscillatory pulses. These waveforms are well correlated and aligned along straight lines that define an average apparent propagation velocity of 582 ± 60 m/s for PRN27 and 660 ± 61 m/s for PRN31. We also computed the propagation velocity using a "slant-stack" technique [e.g., *Calais et al.*, 2003], which estimates the optimal moveout velocity by maximizing the signal-to-noise ratio of time-shifted TEC time series. We find similar horizontal

Figure 4. TEC traces for all sites and satellite (top) PRN27 and (bottom) PRN31 filtered between 2.2 and 8 mHz. Sites are sorted by distance of the SIP to the SHV at explosion time. The distance from the SIP to the SHV at the approximate arrival time is indicated in kilometers underneath each trace. If the satellite was not visible at 3.35 UT (shown as a vertical dotted line), distance is taken from the location of the first SIP. The acoustic perturbation commences after the explosion and is clearly distinguishable from the noise (σ = 0.025 TECU) before the explosion.

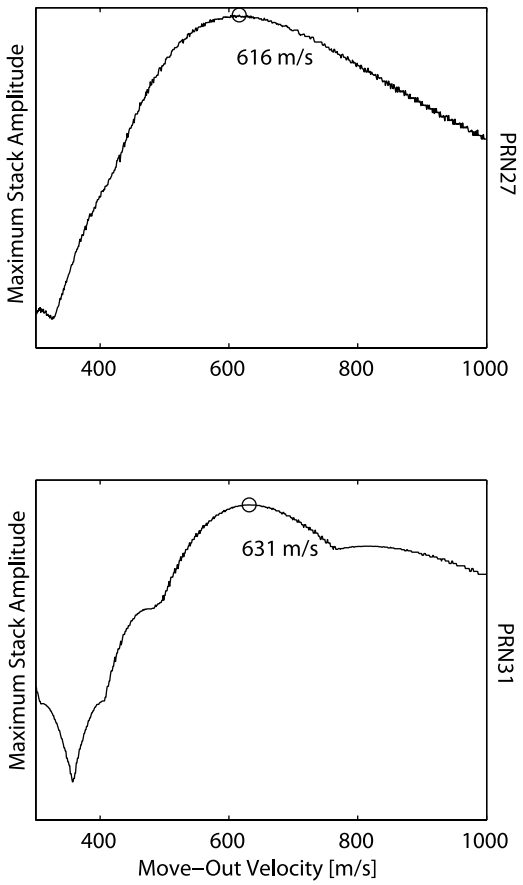

Figure 6. Results of the slant-stack procedure. The apparent horizontal velocity of the TEC perturbation is 612 m/s for PRN27 and 638 m/s for PRN31.

propagation velocity values of 616 m/s and 631 m/s for PRN27 and PRN31 respectively (Figure 6).

[14] TEC measurements are integrated over satellite to ground receiver line of sights, thus they provide no vertical resolution. They are, however, mostly sensitive to perturbations at the maximum electron density in the F2 layer (325 km height, from the International Reference Ionosphere [*Bilitza*, 2001]). Sound speed at that altitude is 735 m/s (MSIS-E-90 Atmosphere Model [*Hedin*, 1987, 1991]); accordingly the difference between the observed (horizontal) propagation velocity implies a vertical propagation component at an elevation angle of approximately 33 degrees ($\cos^{-1}(616/735) \approx 33°$ for PRN27 and $\cos^{-1}(631/735) \approx 33°$ for PRN31). Our ray-tracing propagation model (described below, see Figure 8, left) shows a takeoff angle of 30° at a distance of about 250 km from the source (average distance used in the slant-stack mentioned above), consistent with this simple estimate.

[15] To further illustrate the propagation of the acoustic perturbation while maximizing signal-to-noise ratio, we stacked the TEC time series using clusters of sites. We computed the associated spectrograms (Figure 7) using a Hamming window width of 30 min and 29 min overlap between consecutive windows. All spectrograms show two energy peaks at ~1 mHz and ~4 mHz, as previously identified on individual time series (Figure 3b). The acoustic perturbation after the explosion is visible at 4 mHz, with an arrival time that increases with distance from Montserrat. The 4 mHz peak found here in the TEC perturbation is consistent with previous observations of explosion-induced acoustic perturbations [e.g., *Kanamori and Mori*, 1992; *Delclos et al.*, 1990]. In addition, time series spectrograms (Figure 7) show higher frequencies arriving shortly after the explosion and lower frequencies persisting for a longer time until finally trailing off. This is particularly visible at short distances from the source (Figure 7, middle and top) and illustrates the dispersive nature of the acoustic perturbation. A similar observation was made by *Calais et al.* [1998] using GPS TEC after large mine blasts, but was left unexplained.

[16] In summary, the ionospheric perturbation described above has arrival times, frequency content, propagation speed, and dispersive waveform characteristics that are consistent with it being triggered by the primary SHV explosion of 13 July 2003. Unfortunately, the lava dome collapse, the large explosion and pyroclastic flows knocked out major parts of the GPS equipment and power supply on the island, therefore the data following the first explosion is even more sparse. A preliminary search has not shown any significant ionospheric TEC perturbation after the subsequent explosions (Figure 2) in data from the permanent sites on Puerto Rico. Additionally, because of satellite geometry, the coverage in the maximum coupling area was rather poor.

[17] In the following sections, we will further quantify and test this hypothesis by modeling the acoustic wave propagation using a ray-tracing technique combined with a simplified dispersion model.

3. Modeling

[18] To model the TEC perturbation created by the acoustic wave caused by the explosive eruption of the SHV, we proceed through a series of steps.

[19] 1. We first perform acoustic ray tracing in a horizontally stratified atmosphere model (MSIS-E-90). This computation yields the path of acoustic waves and their arrival times at each point along this path.

[20] 2. Starting with a given velocity source function, we compute its time evolution along each ray using a dispersion relation for acoustic atmospheric waves. We calculate the signal amplitude at each point on the ray assuming energy conservation. We vary the rate of dispersion b and a source amplitude scaling factor C as input parameters to find the best fit to the recorded data.

[21] 3. Once the raypaths and signal amplitude are obtained, we compute, at each epoch and for each satellite-receiver pair, the intersection of each ray with the satellite-receiver line of sight (LoS).

[22] 4. At each intersection, we compute electron density perturbations from the neutral particle velocity using from the momentum equation of magnetohydrodynamics (collision interaction) and the continuity equation for charges.

[23] 5. We then integrate these perturbations along each LoS using the trapezoid rule to obtain a synthetic TEC value.

[24] 6. The synthetic TEC is finally filtered within the same frequency band as the observed TEC to compare with the acoustic part of the observed TEC perturbation.

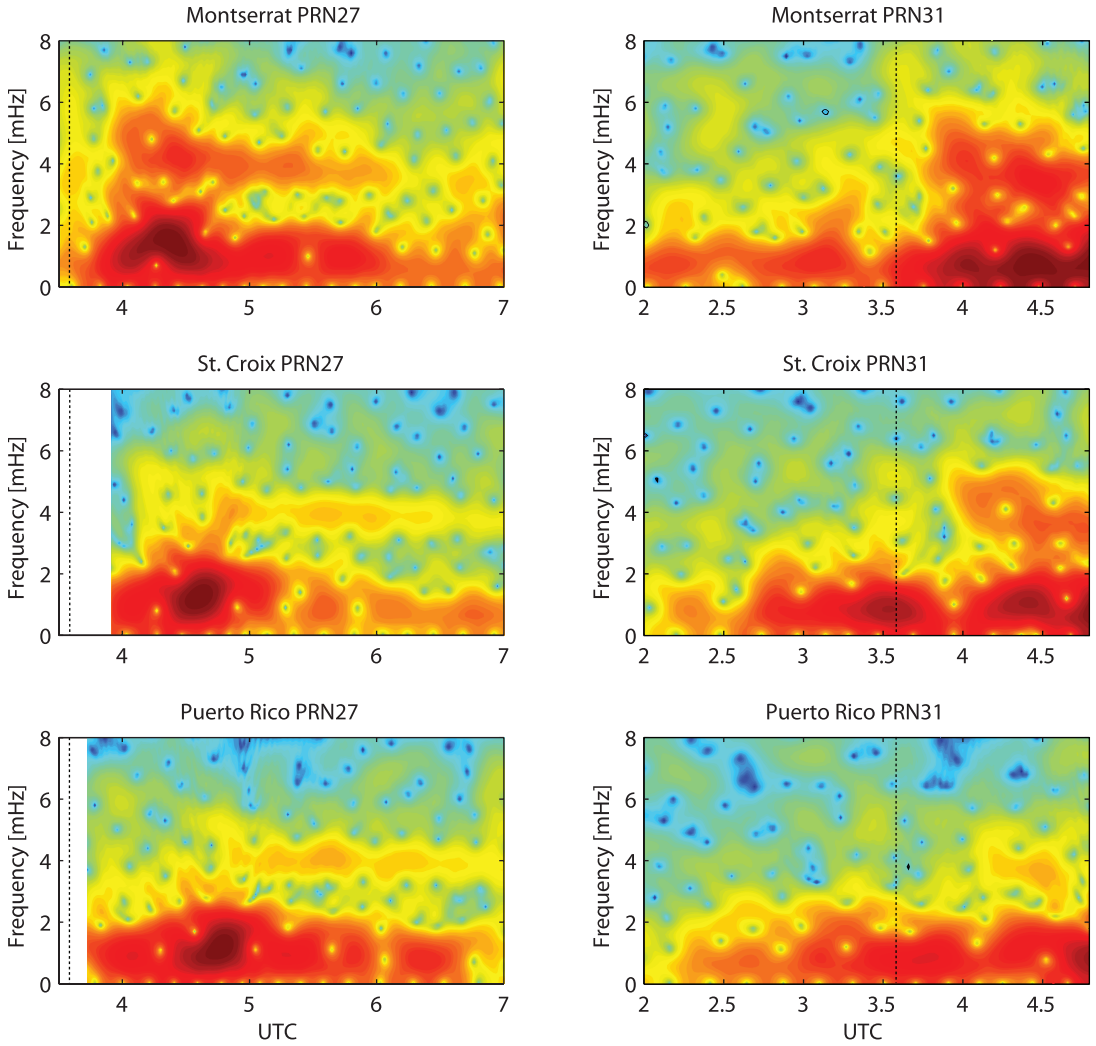

Figure 7. Spectrograms of TEC traces stacked by groups of neighboring GPS stations: top = HERM, SOUF, and MVO1 on Montserrat, middle = CRO1 on St. Croix, and bottom = UPRR and UPRH on Puerto Rico. Left spectrograms correspond to satellite PRN27; right, to PRN31. The vertical dotted line indicates the SHV explosion time. The moveout and fade-out of the perturbation at ≈4 mHz is visible.

3.1. Raytracing

[25] We assume that the explosion can treated, to first order, as a point source located at the center of SHV dome, generating a pressure perturbation that propagates vertically and laterally. We simulate the pressure wave by a set of 180 rays launched at takeoff angles from 0° to 90° [e.g., *Brokešová*, 2006; *Virieux*,1996]. Raypaths depend on the atmospheric refractive index, which is proportional to sound speed. Here we used the MSIS-E-90 atmospheric model (Figure 8, blue line [see also *Hedin*, 1987, 1991]) with a solar flux of 130.7 $Wm^{-2}Hz^{-1}$ and an A_p index of 12 (from http://spidr.ngdc.noaa.gov) at the time and location of the SHV explosion. We trace the acoustic perturbation to a distance and an altitude of 1000 km from the source. At each point of the ray, we obtain the propagation direction and arrival time of the acoustic perturbation.

[26] Conservation of energy and geometric spreading dictate the evolution of the perturbation amplitude along the ray. From the transport equation, amplitude outside of caustics changes between two points $\vec{r}_I$ and $\vec{s}_0$ along the ray as

$$A(\vec{r}_I) = A(\vec{s}_0)\sqrt{\frac{\rho(\vec{s}_0)c_s(\vec{s}_0)J(\vec{s}_0)}{\rho(\vec{r}_I)c_s(\vec{r}_I)J(\vec{r}_I)}} \tag{3}$$

where ρ and c_s are density and sound speed, respectively. J is the ray Jacobian, whose square root $\sqrt{J}$ describes geometric spreading, i.e., variation of the distance between adjacent rays [see details for instance in the study of *Brokešová*, 2006]. We can ignore caustics because they all occur below the ionosphere, as shown in Figure 8 and therefore have negligible impact on TEC. We choose point $\vec{s}_0$ in close proximity to the source (ray position 0.1 s after the explosion). Point $\vec{r}_I$ is always located at the intersection between a ray and a satellite-receiver line of sight. We will treat amplitude $A(\vec{s}_0)$ as an adjustable parameter to match the data.

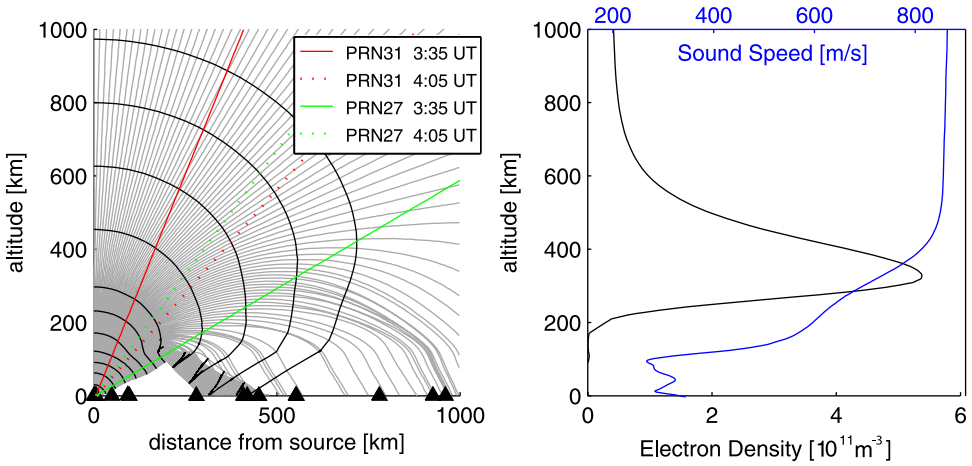

Figure 8. Ray-tracing model. (left) Raypaths (gray lines) computed for the MSIS-E-90 atmosphere profile. The source is at (0, 0). Black triangles show the location of the GPS stations used here. Green and red lines show the lines of sight for satellites PRN27 and PRN31, respectively. Given the altitude of the GPS satellites (about 20,200 km), line of sight from any GPS station would be parallel to the ones shown here. Thick solid black lines show contour of equal arrival time. (right) Sound speed (blue) and electron density (black) profiles used in the model. Sound speed is obtained from MSIS-E-90 and electron density from International Reference Ionosphere [*Bilitza*, 2001] for 13 July 2003 at Montserrat.

[27] The ray amplitude is then convolved with a source function. Following *Fitzgerald* [1997], *Calais et al.* [1998] and *Afraimovich et al.* [2001], we choose to describe the source as a time-dependent velocity perturbation $v(t)$ that follows an "N-wave" shape (first derivative of a Gaussian):

$$v(t) = \frac{\sqrt{2}}{\sigma^{3/2}\pi^{1/4}}(t - t_0)e^{-\frac{(t-t_0)^2}{\sigma^2}} \tag{4}$$

where t_0 is time of maximum displacement and σ^2 describes the width, or variance, of the pulse. We normalize $\int v^2(t)dt = C^2$ and use C to scale $A(\vec{s}_0)$ and match our TEC observations.

3.2. Dispersion

[28] We use the following atmospheric dispersion relation:

$$\omega = \left[\frac{1}{2}\xi^2 c_s^2 \pm \sqrt{\frac{\xi^4 c_s^4}{4} - k_x^2\omega_g^2}\right]^{\frac{1}{2}} \tag{5}$$

with

$$\xi^2 = k_z^2 + k_x^2 + \frac{\omega_a^2}{c_s^2} \tag{6}$$

and the + sign corresponding to acoustic waves. This relation is valid for a slowly varying atmosphere where the temperature gradient does not exceed 7 K/m [*Beer*, 1974]. The maximum temperature gradient in the atmosphere model used here is 0.0152 K/m, well below this boundary.

[29] For a nonisothermal atmosphere with a temperature profile $T = T(z)$, adiabatic constant $\gamma(z) = C_p/C_v$ gravitational acceleration $g(z)$ and sound speed profile $c_s(z)$, the acoustic cutoff frequency ω_a is given by

$$\omega_a = \sqrt{\left(\frac{\gamma g}{2c_s}\right)^2 + \frac{\gamma}{2}\frac{g}{T}\frac{\partial T}{\partial z}} \tag{7}$$

and the Brunt-Vaisala frequency ω_g by

$$\omega_g = \sqrt{\frac{(\gamma - 1)g^2}{c_s^2} + \frac{g}{T}\frac{\partial T}{\partial z}} \tag{8}$$

The Nyquist frequency for the GPS data used here, sampled at $T_s = 30$ s, is $f_N = (2T_s)^{-1} = 16$ mHz. To avoid aliasing, we are limited to half the Nyquist frequency, or 8 mHz, corresponding to an average wave number k:

$$k \approx \frac{1}{\lambda} = \frac{f}{\bar{c}_s} = 1.23 \times 10^{-5}\, m^{-1} \ll 1 \tag{9}$$

where we have used the average sound speed of our atmosphere profile, $\bar{c}_s = 651.52$ m/s. Since k is small, we expand the dispersion relation (equation (5)) into a second-order Taylor series in k_x and k_z around $k_x = k_z = 0$:

$$\omega = \omega_a + \frac{1}{2}b_z k_z^2 + \frac{1}{2}b_x k_x^2 \tag{10}$$

with

$$b_z = \frac{c_s^2}{\omega_a} \tag{11}$$

and

$$b_x = \frac{c_s^2 - \frac{\omega_g^2}{\omega_a^2}}{\omega_a} \tag{12}$$

Since $(\omega_g/\omega_a)^2 \ll 1$, we set $b_z = b_x$ and $k^2 = k_z^2 + k_x^2$, so that equation (10) reduces to

$$\omega(k) = \omega_a + \frac{1}{2} b_x k^2 \tag{13}$$

We insert this dispersion relation (equation (13)) into the Fourier integral of the displacement $s(t)$ given by

$$s(x,t) = \int_{-\infty}^{\infty} a(k) e^{-i(kx - w(k)t)} dk \tag{14}$$

Velocity can obviously be derived from displacement s at any location x and time t using $v(x, t) = ds(x, t)/dt$. $s(x, t)$ is taken as a Gaussian pulse (see above) so that the amplitude distribution $a(k)$ in k space is

$$a(k) = A \frac{1}{\sqrt{4\pi\sigma_k^2}} e^{-\frac{(k-k_0)^2}{2\sigma_k}} \tag{15}$$

The pulse hence broadens as a function of time as a result of dispersion. We calculate the time dependency of the pulse width in space using its variance:

$$\sigma^2 = \int_{-\infty}^{\infty} (x-\mu)^2 |s(x-\mu, t)| dx \tag{16}$$

which leads to the standard deviation

$$\sigma = \sqrt{\underbrace{\frac{\pi^{1/2} A^2}{4\sigma_k^3}}_{a} + \underbrace{\frac{3A^2 \pi^{\frac{1}{2}} k_0^2 b_z^2}{4\sigma_k}}_{b} t^2} \tag{17}$$

which is of the form

$$\sigma = \sqrt{a + bt^2}. \tag{18}$$

Parameter a is the initial standard deviation of the source function at $t = 0$, while b parameterizes the broadening of the pulse as the acoustic wave propagates.

[30] When the pulse propagates past a given location $\vec{x}$ while it is spreading, the resulting time series shows a steep increase followed by a gradual return to equilibrium. Inserting $\sigma(t_{arrival} + t)$ into equation (4) accurately describes the spread of $s(t)$ at a given location $\vec{x}$, where $t_{arrival}$ is the arrival time at that location. There is a tradeoff between parameters a and b since a long-pulse duration at the source and a small spread rate will have the same effect as a short pulse and a large spread rate. From infrasonic observations (e.g., *Johnson* [2003] for an overview), we know that pressure waves detected close to volcanic explosions have a duration of about 1 s or less. To minimize computation time we choose a to be one second and adjust parameters b (dispersion) and C (amplitude scaling) to match the data.

[31] We now have the shape and amplitude of the synthetic waveform at the intersection between rays and satellite-receiver line of sights and can proceed to calculate the electron density perturbation caused by the neutral pressure wave.

3.3. Electron Density Perturbation

[32] We compute electron density perturbations assuming that ionospheric charged particles follow the motion of neutral gas through collision interaction [*Davies and Archambeau*, 1998]. The interaction can be described by the Navier-Stokes equation of magnetohydrodynamics [*Boyd and Sanderson*, 2003]:

$$\rho_e \frac{d\vec{v}_e}{dt} = -\nabla p + \rho_e \vec{g} + Ne\left(\vec{E} + \vec{v}_e \times \vec{B}\right) - \rho_e \nu_{en}(\vec{v}_e - \vec{u}) \tag{19}$$

The electron velocity $\vec{v}_e$ is obtained by solving equation (19) using a finite difference scheme, with the neutral particle velocity $\vec{u}$ as input. Additional parameters in the equation are the hydrostatic pressure gradient ∇p (assumed to be nonzero in the z direction only), specific gravity $g(z)$, electron mass density ρ_e, electron number density N, electron charge e, Earth's magnetic field B and the neutral-electron collision frequency ν_{en}. We neglect the electric force $e\vec{E}$, since the electric field is small in the ionosphere ($\approx 10^{-8}$ Vm^{-1}, *Reid* [1965]) and the dynamics are largely governed by the magnetic field. All the other parameters are either physical constants or can be obtained from external models, described below after the coupling procedure.

[33] Assuming that the total charge remains constant, the continuity equations is

$$\frac{\partial N}{\partial t} + \nabla \cdot (N\vec{v}_e) = 0 \tag{20}$$

Integrating over time on both sides while assuming that electron density is horizontally stratified yields the perturbation δN to the ambient electron density N at the position $\vec{r}_I$ (intersection point between satellite-receiver line of sight and acoustic ray):

$$\delta N(\vec{r}_I, t) = -\frac{\partial N}{\partial z} \int_{t_{arrival}}^{t} v_{e,z}(\vec{r}_I, \hat{t}) d\hat{t} - N(z) \int_{t_{arrival}}^{t} \nabla \cdot \vec{v}_e(r_I, \hat{t}) d\hat{t} \tag{21}$$

where we have assumed that electron density perturbations are small so that the $\partial N/\partial z$ and $N(z)$ terms can be taken outside the integral. We compute the electron density perturbation (equation (21)) from time $t_{arrival}$ when the perturbation reaches the point $\vec{r}_I$ to the time of the TEC observation t.

[34] We use magnetic field vectors $\vec{B}$ from the International Geomagnetic Reference Field IGRF-10 ([*Maus and Macmillan*, 2005] http://www.ngdc.noaa.gov/seg/geomag/magfield.shtml) The initial electron distribution N is taken from the International Reference Ionosphere [*Bilitza*, 2001]

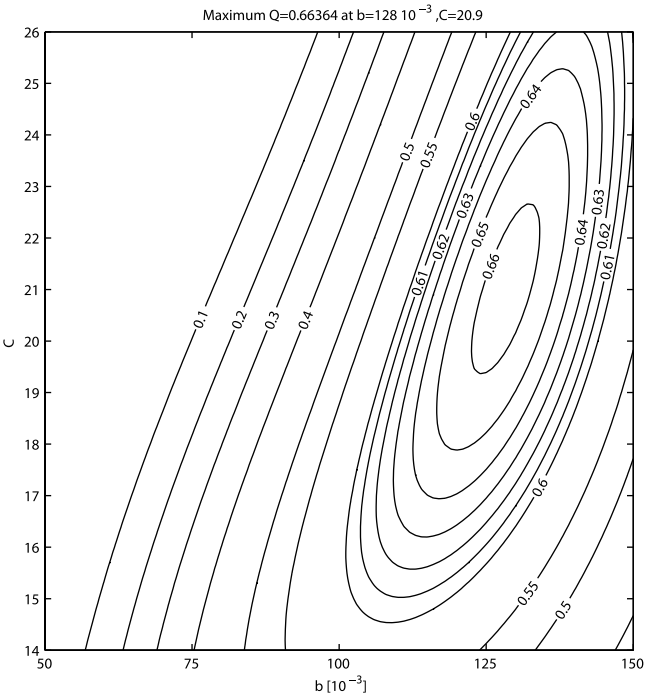

Figure 9. Grid search result in (C, b) space. All stations and satellites PRN27 and PRN31 are taken into account. Contours show χ^2 probability assuming a constant measurement error of 0.0249 TECU. Values within the 0.66 contour correspond to uncertainty in the derived parameters b and C.

for the coordinates and explosion time of the SHV on 13 July 2003 (Figure 8, right, black line). The electron density distribution is assumed to be constant in north-south and east-west direction and variable with altitude, $N = N(z)$.

[35] For collisions we only consider the most abundant neutral gasses at ionospheric altitudes, neutral oxygen O and molecular nitrogen N_2 [see *Kelley*, 1992, Figure 1.2]. We compute neutral atmosphere-electron collision frequencies ν_{en} based on the equations given by *Schunk and Nagy* [1980; Table 3]:

$$\nu_{en} = N_O 8.9 \cdot 10^{-11}\left(1 + 5.7 \cdot 10^{-4} T_e\right) T_e^{1/2} + N_{N_2} 2.33 \cdot 10^{-11}\left(1 - 1.21 \cdot 10^{-4} T_e\right) T_e \quad (22)$$

with the electron temperature T_e as provided from International Reference Ionosphere, the number densities for neutral oxygen N_O and molecular nitrogen N_{N2} from the aforementioned MSIS-E-90 atmosphere profile.

[36] Once electron density perturbations are computed at every intersection j between acoustic rays and satellite-receiver line of sights, we integrate the electron density perturbations δN_j, $j = 1, \ldots, n$ using the trapezoid rule:

$$TEC = \sum_{j=1}^{n} \frac{1}{2}\left(l_{j+1} - l_j\right)\left(N_{j+1} + N_j\right) \quad (23)$$

and obtain a synthetic TEC value. This procedure constitutes a complete three-dimensional model which includes the aspect dependence of TEC perturbations, as for example described by *Afraimovich et al.* [1992, 1998].

3.4. Results

[37] The synthetic TEC time series are filtered in the same manner as the observed ones. We estimate unknown parameters b, and C using a grid search algorithm in this 2-parameter space, evaluating the fit between observed and modeled TEC time series with a chi-square function defined as

$$\chi^2 = \sum_{i=1}^{M} \left(\frac{y_i - y(b, C)}{\sigma_i}\right)^2 \quad (24)$$

where y_i is the observed value, $y(b, C)$ the modeled value, and σ_i the measurement uncertainty of each y_i for $i = 1, \ldots, M$, where M is the total number of individual TEC samples. We chose for y_i the envelope of the recorded data and for $y(b, C)$ the envelope of the modeled filtered TEC.

[38] Assuming a constant measurement error $\sigma_i = \sigma = 0.0249$ *TECU*, derived from the variance of the observed TEC signal in the 2.2–8 mHz frequency range on 12 July in the absence of the acoustic perturbation, we computed uncertainties in the estimated parameters by calculating the probability $Q(\chi^2, \nu)$ corresponding to each χ^2 value for $\nu = N - 2$ degrees of freedom (since we have two parameters). Q describes the probability that a particular χ^2 value is exceeded by chance. We find a maximum probability of 0.663 for $b = 0.128$ and $C = 21$ (Figure 9). Within 0.66 Q contour, we find that b may vary from 0.123 to 0.134, C from 19.4 to 22.6.

[39] Figures 10 and 11 compare the synthetic TEC perturbation obtained using the best fit values for b, and C with the observed signal for satellites PRN27 and PRN31 in the acoustic frequency band. The amplitude of the synthetic perturbations matches well with the ones observed in GPS TEC. Onset times are in good agreement between synthetics and observed time series, and the observed moveout is well reproduced. Initial oscillations in the synthetic time series are however of smaller amplitudes than observed.

4. Discussion

4.1. Frequency Content

[40] The frequency content of the acoustic TEC perturbation recorded here is consistent with atmospheric perturbations after other volcanic eruptions. For instance, *Kanamori and Mori* [1992] report an atmospheric oscillation after the 1991 Pinatubo eruption with periods of 230 s and 270 s (4.3 mHz and 3.7 mHz). *Delclos et al.* [1990] find similar signals after the 1980 Mt. St Helens eruption, with periods of 210 s and 330 s (4.5 mHz and 3 mHz). Using a fluid dynamics approach, *Kanamori et al.* [1994] show that these components are acoustic resonant frequencies determined by temperature inversions around 30 km and 100 km height. This was further confirmed by *Watada* [1995] and *Lognonné et al.* [1998], who computed normal modes of the Earth-atmosphere system and showed that sources at ground level excite atmospheric modes at resonant frequencies of 3.7 mHz and 4.4 mHz.

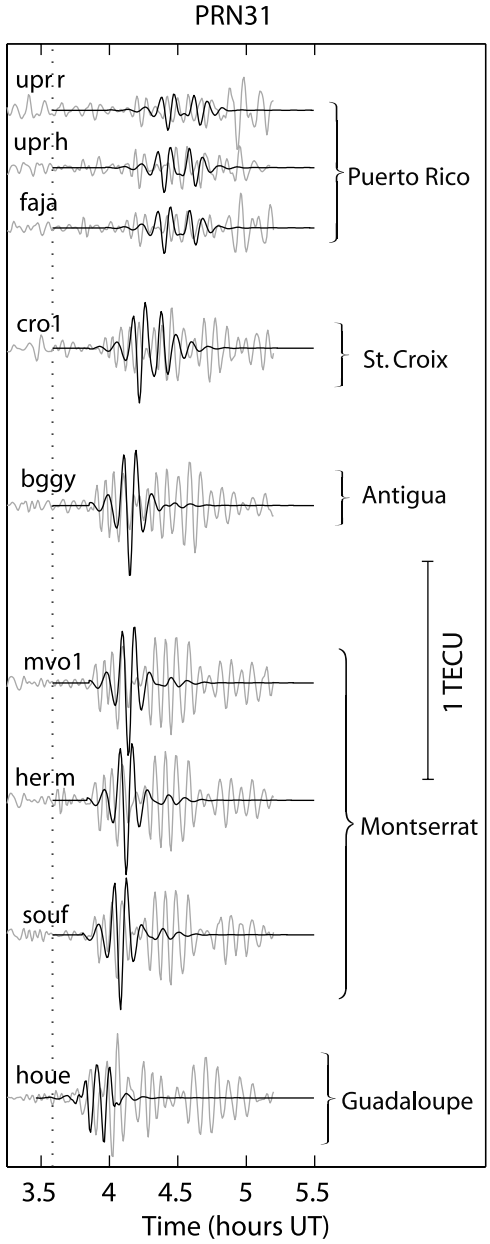

Figure 10. Synthetic (black) versus observed (gray) TEC time series for PRN31, filtered between 2.2 and 8 mHz. Synthetics were computed for $a = 1$ s, $b = 124 \times 10^{-3}$, and $C = 21$.

[41] The maximum energy of the observed gravity wave (1.2 mHz, Figure 7) coincides with the arrival time of the acoustic component. However, PRN31, for which data is available for 1.5 hour before the explosion, shows a gravity component preceding the explosion, whereas no acoustic signal is yet present. The acoustic component is therefore clearly linked to the explosion, while part of the observed gravity component must be due to processes that predate the explosion. A candidate process is the tsunami triggered by a large pyroclastic flow that reached the ocean around 22:00 UT on 12 July [*Mattioli et al.*, 2007]. Tsunami waves are known to couple efficiently with the atmosphere in the 0.8–1.7 mHz frequency range and have been previously recorded from GPS TEC data in Japan by *Artru et al.* [2005] and modeled by *Occhipinti et al.* [2006]. Alternatively, convective processes such as the ash plume from a volcanic explosion are known to cause long-period gravity waves in the ionosphere, as described theoretically by *Townsend* [1966].

4.2. Dispersion Characteristics

[42] "Nondispersive" models for the propagation of explosion-triggered acoustic waves predict arrival times well [e.g., *Warshaw and Dubois*, 1981; *Fitzgerald*, 1997; *Heki*, 2006]. The perturbation waveform consists of a simple pulse (depending on the source function used, generally a *N* wave), which matches the data well at least at large distances from the source. However, these models fail to explain the long duration oscillatory signal and complex waveform recorded after large events or at short distances to the source, such as the observations reported in

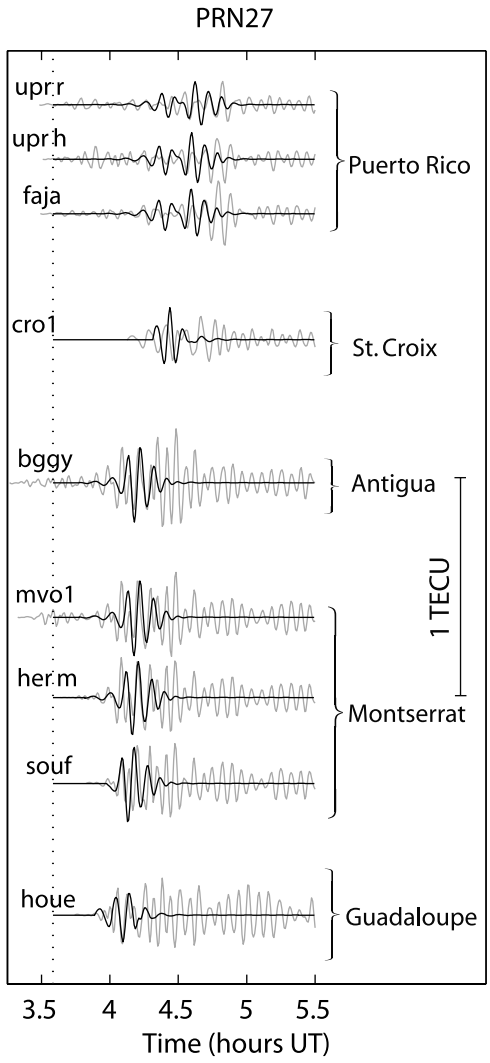

Figure 11. Synthetic (black) versus observed (gray) TEC time series for PRN27, filtered between 2.2 and 8 mHz. Synthetics were computed for $a = 1$ s, $b = 124 \times 10^{-3}$, and $C = 21$.

Table 1. Explosion Energy Reported for Previous Events[a]

Event	Date	VEI	Energy ($10^{12}J$)	Type	Reference
Mine Blast	19 Jul 1996		6.3	total	*Calais et al.* [1998]
Chemical Explosion	10 Jul 1993		8.5	total	*Massey et al.* [1994]
Unzen Volcano	1991	1	280	acoustic	*Taniguchi and Suzuki-Kamata* [1993]
Asama Volcano	01 Sep 2004	2	200	total	*Heki* [2006]
Asama Volcano	01 Sep 2004	2	1.2×10^{-5}	acoustic	*Heki* [2006]
Soufrière Hills	2003	3	1.5×10^{-2}	acoustic	this publication
Pelee	1902	4	300	acoustic	*Woulff and McGetchin* [1976]
Shiveluch	1965	4	140	acoustic	*Woulff and McGetchin* [1976]
Tolbachik	uknw	4	10^{-4}	acoustic	*Johnson* [2003]
Bezymianny	1956	5	3×10^{3}	acoustic	*Woulff and McGetchin* [1976]
Krakatoa	1883	6	8.6×10^{4}	acoustic	*Woulff and McGetchin* [1976]

[a]VEI is the volcanic explosivity introduced by *Newhall and Self* [1982]. VEI values where obtained from the Smithsonian Institution-Global Volcanism Program (www.volcano.si.edu).

this paper. *Calais and Minster* [1998] tried to explain the oscillatory TEC signal triggered by a rocket launch by invoking guided waves ducted by the temperature inversion at 100 km altitude. Their approach produced oscillatory TEC signals but failed to explain the dispersion visible in the TEC spectrograms. Theoretical calculations [e.g., *Landau and Lifshitz*, 1959; *Beer*, 1974] do show that the atmosphere is slightly dispersive at acoustic frequencies. Since this effect is small (i.e., $\omega \sim ck$ in equation (5), resulting in a phase speed very close to the group velocity) it is usually neglected in propagation models for TEC perturbations. This simplification is justified for explosive events of low energy (or recorded at large distances from the source) because viscous strain quickly attenuates low-amplitude wave trains below measurement noise. It does not hold, however, for high-energy events, in particular when observations are available from near-field stations, as shown here.

[43] Considering the simplified model used here, synthetic waveforms match the data reasonably well. The fact that our model fails to reproduce the long-lasting oscillatory tail observed in the data suggests a source more complex than the simple N wave used here, perhaps consisting of several pulses. Indeed, *Mattioli et al.* [2007] used bore hole strain and seismic data with much higher sampling frequency than the GPS TEC measurements reported here to reconstruct the details of the dome collapse. They show that although the peak in seismic and strain energy is temporally aligned with the largest explosion (as modeled above), significant dome collapse continued well after 3:35 UTC. Unfortunately no near-field pressure data is available at a sample rate high enough to independently constrain the source function.

4.3. Acoustic Energy Release

[44] Once the model is calibrated and the propagation and source parameters calculated, we compute the total acoustic energy of the explosion by integrating energy density $e = \rho v(t)^2$ over the total model volume from the source up to 1000 km altitude and 1000 km radial distance from the SHV and at each GPS sampling interval. The integration results in an average value for the acoustic energy release of $E_{acoustic} = (1.53 \pm 0.1) \times 10^{10}$ J, where we have taken the standard deviation over all energy values as the uncertainty.

[45] The only other attempt, to our knowledge, to derive explosion energy from GPS-derived TEC perturbation was by *Heki* [2006] for the 2004 eruption of the Asama volcano in Japan. The author calculates energy using

$$E_{acoustic} = \frac{2\pi r^2}{\rho c} \int \Delta P^2(t) dt \tag{25}$$

a relation commonly used in infrasound studies to compute acoustic energy from barographic oscillations [e.g., *Johnson*, 2003]. The derivation of equation (25), however, assumes spherical symmetry in the propagation of the pressure pulse as well as constant mass density and sound speed. These simplifications are appropriate in the lower atmosphere but break down as the pressure wave propagates to higher altitudes where ray bending becomes significant.

[46] As expected, equation (25) returns an acoustic energy of 1.5×10^{10} J from model rays sampled near the source. However, the energy estimated from equation (25) varies between a maximum of 2×10^{10} J at 122 km (maximum sound speed gradient) and a minimum of 0.3×10^{10} J at 1000 km (minimum density). At the F layer peak (maximum electron density), the energy calculated using equation (25) is 0.75×10^{10} J, half of the value computed using the ray-tracing model. Since *Heki* [2006] used equation (25) (assuming that the TEC perturbations are proportional to the relative change in ambient pressure at the height of the F layer, 300 km in his case) and neglected geometric spreading, his estimate of the acoustic energy released by the Asama volcanic explosion is probably underestimated by ~50%.

[47] Estimates of energy release by volcanic explosions based on seismic observations have been reported by numerous authors but estimates of the corresponding acoustic component remain sparse. *Pyle* [2000, Table 1] provides a summary of thermal and seismic energy for a number of large volcanic explosions. We note, however, that *Hedervari* [1963] showed that acoustic energy can vary as a fraction from 1/100 to 1/1000 of the thermal energy. In Table 1 we summarize the few values we were able to find for acoustic and total energy from artificial and natural explosions. They vary over a wide range, the lowest being the one reported by *Heki* [2006], the largest the one reported by *Woulff and McGetchin* [1976] for the 1883 Krakatoa eruption. Correlation between acoustic energy and volcanic explosivity index (VEI) is not simple, but we note that our estimate

for the 2003 SHV explosion fits within the range of published values for explosions of similar magnitude.

5. Conclusions

[48] We have developed a technique to compute TEC perturbations triggered by acoustic sources and applied it to estimate the acoustic energy associated with the explosive dome collapse of the SHV on 13 July 2003. Previous studies of atmospheric acoustic waves triggered by earthquakes or explosions have neglected the dispersion characteristics of atmospheric perturbation. This simplification, justified for explosive events of low energy (or recorded at large distances from the source) does not hold for high-energy events, as observed when data are available from near-field stations. Accounting for dispersion of the acoustic perturbations allows us to match the observed waveforms reasonably well. Further refinement of the source function, accounting for a series of explosions rather than a single impulsive event, may help improve the fit to the observed perturbation. We show that the acoustic energy can be estimated by matching observed an synthetic waveforms and illustrate the importance of accounting for geometric spreading when estimating source energy from GPS TEC.

[49] Our modeling approach includes a number of simplifications. The raytracing part neglects winds as well as temperature and density deviations from the MSIS-E-90 atmosphere model, which can have a significant impact on the timing and propagation paths of atmospheric acoustic waves [*Argo et al.*, 1995]. However, the HWM-93 empirical wind model [*Hedin et al.*, 1996] yields a maximum wind to sound speed ratio of only 10.9% at 255 km altitude over the location of Montserrat and for the environmental conditions at the time of the eruption.

[50] Localized turbulence or anomalous temperature gradients may also cause a focusing or defocusing of the acoustic rays. In those cases, rays may cross and cause additional caustics, leading to unaccounted attenuation or amplification of the acoustic waves.

[51] Thanks to the growing number of continuous GPS sites all across the globe and the availability of data from dense GPS networks, the method proposed here can be used to quantify acoustic energy release by any source that generates acoustic waves. Stacking raw observations from a large number of GPS receivers [*Calais et al.*, 1998] may help lower the detection threshold and allow the study of lesser magnitude events.

[52] **Acknowledgments.** We thank the NSF-EAR CD and IF programs for continued support of the CALIPSO facility (NSF-IF0523097 and NSF-IF-0732728) and analysis of data derived therefrom (NSF-CD-0607782). We thank Associate Editor P. Elosegui and reviewers K. Heki and E. Afraimovitch for their insightful comments.

References

Afraimovich, E. L., A. I. Terekhov, M. I. Ududov, and S. V. Fridman (1992), Refraction distortions of transionospheric radio signals caused by changes in a regular ionosphere and by travelling ionospheric disturbances, *J. Atmos. Terr. Phys.*, *54*, 1013–1020.

Afraimovich, E. L., K. S. Palamartchouk, and N. P. Perevalova (1998), GPS radio interferometry of travelling ionospheric disturbances, *J. Atmos. Sol. Terr. Phys.*, *60*, 1205–1223.

Afraimovich, E. L., N. P. Perevalova, A. V. Plotnikov, and A. M. Uralov (2001), The shock-acoustic waves generated by earthquakes, *Ann. Geophys.*, *19*, 395–409.

Argo, P., R. A. Clark, A. Douglas, V. Gupta, J. Hassard, P. M. Lewis, P. K. H. Maguire, K. Playford, and F. Ringdal (1995), The detection and recognition of underground nuclear explosions, *Surv. Geophys.*, *16*, 495–532, doi:10.1007/BF00665683.

Artru, J., V. Ducic, H. Kanamori, P. Lognonné, and M. Murakami (2005), Ionospheric detection of gravity waves induced by tsunamis, *Geophys. J. Int.*, *160*, 840–848.

Beer, T. (1974), *Atmospheric Waves*, John Wiley, New York.

Bilitza, D. (2001), International reference ionosphere 2000, *Radio Sci.*, *36*, 261–275.

Blanc, E. (1985), Observations in the upper atmosphere of infrasonic waves from natural or artificial sources—A summary, *Ann. Geophys.*, *3*, 673–687.

Boyd, T. J. M., and J. J. Sanderson (2003), *The Physics of Plasmas*, Cambridge Univ. Press.

Brokešová, J. (2006), *Asymptotic Ray Method in Seismology: A Tutorial*, Matfyzpress, Prague, Czech Republic.

Calais, E., and J. B. Minster (1998), GPS, earthquakes, the ionosphere, and the space shuttle, *Phys. Earth Planet. Inter.*, *105*, 167–181.

Calais, E., J. Bernard Minster, M. Hofton, and M. Hedlin (1998), Ionospheric signature of surface mine blasts from Global Positioning System measurements, *Geophys. J. Int.*, *132*, 191–202.

Calais, E., J. S. Haase, and J. B. Minister (2003), Detection of ionospheric perturbations using a dense GPS array in Southern California, *Geophys. Res. Lett.*, *30*(12), 1628, doi:10.1029/2003GL017708.

Davies, J. B., and C. B. Archambeau (1998), Modeling of atmospheric and ionospheric disturbances from shallow seismic sources, *Phys. Earth Planet. Inter.*, *105*, 183–199.

Delclos, C., E. Blanc, P. Broche, F. Glangeaud, and J. L. Lacoume (1990), Processing and interpretation of microbarograph signals generated by the explosion of Mount St. Helens, *J. Geophys. Res.*, *95*, 5485–5494.

Fitzgerald, T. J. (1997), Observations of total electron content perturbations on GPS signals caused by a ground level explosion, *J. Atmos. Terr. Phys.*, *59*, 829–834.

Georges, T., and W. Hooke (1970), Wave-induced fluctuations in ionospheric electron content: A model indicating some observational biases, *J. Geophys. Res.*, *75*, 6295–6308.

Hedervari, P. (1963), On the energy and magnitude of volcanic eruptions, *Bull. Volcanol.*, *25*(1), 373–385.

Hedin, A. E. (1987), MSIS-86 thermospheric model, *J. Geophys. Res.*, *92*, 4649–4662.

Hedin, A. E. (1991), Extension of the MSIS thermosphere model into the middle and lower atmosphere, *J. Geophys. Res.*, *96*, 1159–1172.

Hedin, A. E., et al. (1996), Empirical wind model for the upper, middle and lower atmosphere, *J. Atmos. Terr. Phys.*, *58*, 1421–1447.

Heki, K. (2006), Explosion energy of the 2004 eruption of the Asama Volcano, central Japan, inferred from ionospheric disturbances, *Geophys. Res. Lett.*, *33*, L14303, doi:10.1029/2006GL026249.

Heki, K., and J. Ping (2005), Directivity and apparent velocity of the coseismic ionospheric disturbances observed with a dense GPS array, *Earth Planet. Sci. Lett.*, *236*, 845–855, doi:10.1016/j.epsl.2005.06.010.

Herd, R. A., M. Edmonds, and V. A. Bass (2005), Catastrophic lava dome failure at Soufrière Hills Volcano, Montserrat, 12–13 July 2003, *J. Volcanol. Geotherm. Res.*, *148*, 234–252.

Johnson, J. B. (2003), Generation and propagation of infrasonic airwaves from volcanic explosions, *J. Volcanol. Geotherm. Res.*, *121*(1–2), 1–14.

Kanamori, H., and J. Mori (1992), Harmonic excitation of mantle Rayleigh waves by the 1991 eruption of Mount Pinatubo, Philippines, *Geophys. Res. Lett.*, *19*, 721–724.

Kanamori, H., J. Mori, and D. G. Harkrider (1994), Excitation of atmospheric oscillations by volcanic eruptions, *J. Geophys. Res.*, *99*, 21,947–21,961.

Kelley, M. C. (1992), *The Earth's Ionosphere*, Elsevier, New York.

Klobuchar, J. A. (1985), Ionospheric time delay effects on earth space propagation, in *Handbook of Geophysics and the Space Evironment*, edited by A. S. Jursa, chap. 10.8, pp. 1084–1088, U.S. Air Force, Washington, D. C.

Landau, L. D., and E. M. Lifshitz (1959), Fluid mechanics, in *Course of Theoretical Physics*, Elsevier, New York.

Lognonné, P., E. Clévédé, and H. Kanamori (1998), Computation of seismograms and atmospheric oscillations by normal-mode summation for a spherical earth model with realistic atmosphere, *Geophys. J. Int.*, *135*, 388–406.

Manucci, A. J., B. D. Wilson, and C. D. Edwards (1993), A new method for monitoring the Earth's ionospheric total electron content using the GPS global network, in *ION GPS-93: Proceedings of the 6th International Technical Meeting of the Satellite Division of the Institute of Navigation*, pp. 1323–1332, Salt Lake City, Utah.

Massey, R. S., R. C. Carlos, A. R. Jacobson, and G. Wu (1994), Observations of TEC fluctuations from an explosion on the Earth's surface, paper

presented at the International Beacon Satellite Symposium, Aberystwyth, Wales, 11–15 Jul., pp. 11–15, Los Alamos National Laboratories.

Mattioli, G. S., et al. (2004), Prototype PBO instrumentation of CALIPSO project captures world-record lava dome collapse on Montserrat volcano, *Eos Trans. AGU*, *85*(34), doi:10.1029/2004EO340001.

Mattioli, G., et al. (2007), Unique and remarkable dilatometer measurements of pyroclastic flow generated tsunami waves, *Geology*, *35*(1), 25–28, doi:10.1130/G22931A.1.

Maus, S., and S. Macmillan (2005), International geomagnetic reference field—The tenth generation, *Earth Planets Space*, *57*(12), 1135–1140.

Mazzella, A. J., E. A. Holland, A. M. Andreasen, C. C. Andreasen, G. S. Rao, and G. J. Bishop (2002), Autonomous estimation of plasmasphere content using GPS measurements, *Radio Sci.*, *37*(6), 1092, doi:10.1029/2001RS002520.

Newhall, C. G., and S. Self (1982), The volcanic explosivity index /VEI/—An estimate of explosive magnitude for historical volcanism, *J. Geophys. Res.*, *87*, 1231–1238.

Occhipinti, G., P. Lognonné, E. A. Kherani, and H. Hébert (2006), Three-dimensional waveform modeling of ionospheric signature induced by the 2004 Sumatra tsunami, *Geophys. Res. Lett.*, *33*, L20104, doi:10.1029/2006GL026865.

Pyle, D. M. (2000), Sizes of volcanic eruptions, in *Encyclopedia of Volcanoes*, edited by H. Rymer, pp. 263–269, Elsevier, New York.

Reid, G. (1965), Ionospheric effects of electrostatic fields generated in the outer magnetosphere, *J. Res. Natl. Bur. Stand. U.S.*, *69D*, 827–837.

Roberts, D. H., J. A. Klobuchar, P. F. Fougere, and D. H. Hendrickson (1982), A large-amplitude traveling ionospheric disturbance produced by the May 18, 1980, explosion of Mount St. Helens, *J. Geophys. Res.*, *87*, 6291–6301.

Sardon, E., A. Rius, and N. Zarraoa (1994), Estimation of the transmitter and receiver differential biases and the ionospheric total electron content from Global Positioning System observations, *Radio Sci.*, *29*(3), 577–586.

Schunk, R. W., and A. F. Nagy (1980), Ionospheres of the terrestrial planets, *Rev. Geophys. Space Phys.*, *18*, 813–852.

Taniguchi, H., and K. Suzuki-Kamata (1993), Direct measurement of over pressure of a volcanic blast on the June 1991 eruption at Unzen Volcano, Japan, *Geophys. Res. Lett.*, *20*, 89–92.

Townsend, A. A. (1966), Internal waves produced by a convective layer, *J. Fluid Mech.*, *24*, 307–319.

Virieux, J. (1996), Seismic ray tracing, in *Seismic Modelling of Earth Structure*, edited by E. Boschi, G. Ekström, and A. Morelli, pp. 223–303, Inst. Naz. Geofis., Rome, Italy.

Warshaw, S., and P. Dubois (1981), Preliminary theoretical acoustic and RF sounding calculations for Mill Race, *Tech. Rep. UCID-19231*, Lawrence Livermore Natl. Lab., Livermore, Calif.

Watada, S. (1995), Part 1: Near source acoustic coupling between the atmosphere and the solid earth during volcanic erruptions, Ph.D. thesis, California Inst. of Technol., Pasadena, Calif.

Widmer, R., and W. Zürn (1992), Bichromatic excitation of long-period Rayleigh and air waves by the Mount Pinatubo and El Chichon volcanic eruptions, *Geophys. Res. Lett.*, *19*, 765–768.

Woulff, G., and T. R. McGetchin (1976), Acoustic noise from volcanoes—Theory and experiment, *Geophys. J. R. Astron. Soc.*, *45*, 601–616.

Yamamoto, R. (1956), The microbarographic oscillations produced by the explosion of hydrogen bombs in the Marshall Islands, *Bull. Am. Meteorol. Soc.*, *37*, 406–409.

Yeh, K. C., and C. H. Liu (1972), *Theory of Ionospheric Waves, International Geophysics Series*, vol. 17, Elsevier, New York.

Zürn, W., and R. Widmer (1996), Worldwide observation of Bichromatic long-Period Rayleigh waves excited during the June 15th, 1991 eruption of Mount Pinatubo, in *Fire and Mud: Eruptions and Lahars of Mount Pinatubo, Philippines*, edited by R. S. Punongbayan and C. G. Newhall, pp. 615–624, Univ. of Washington Press, Seattle, Wash.

E. Calais, Department of Earth and Atmospheric Sciences, Purdue University, 525 Northwestern Avenue, West Lafayette, IN 47907, USA. (ecalais@purdue.edu)

T. Dautermann, Institute of Communications and Navigation, German Aerospace Center (DLR), Oberpfaffenhofen, D-82234 Wessling, Germany. (thomas.dautermann@dlr.de)

G. S. Mattioli, Department of Geosciences, University of Arkansas, 113 Ozark Hall, Fayetteville, AR 72701, USA. (mattioli@uark.edu)